European Journal of Pharmaceutics and Biopharmaceutics 208 (2025) 114632

Contents lists available at ScienceDirect

European Journal of Pharmaceutics and Biopharmaceutics

journal homepage: www.elsevier.com/locate/ejpb

Glow in the dark tumor: Enhanced near-IR visualization and destruction of cancer with a self-quenched theranostic

S. İrem Güler [a,b], Cem Levent Altan [c], E. Esma Demircioglu [a], Nihan Verimli [a,b], Beyza Abisoglu [c], Cigdem Bayraktaroglu [a], Mustafa Caglar Beker [d], S. Sibel Erdem [a,b,*]

[a] Istanbul Medipol University Research Institute for Health Sciences and Technologies (SABITA) Drug Development Center Istanbul Turkey
[b] International School of Medicine Medical Biochemistry Istanbul Medipol University Istanbul Turkey
[c] Department of Chemical Engineering Yeditepe University Atasehir Istanbul Turkey
[d] School of Medicine Department of Physiology Istanbul Medeniyet University Istanbul Turkey

ARTICLE INFO

Keywords:
Superparamagnetic iron oxide nanoparticle
Photodynamic therapy
Theranostic agent
Near-IR imaging
Breast cancer
Fluorescence quenching

ABSTRACT

Late diagnosis is one of the major obstacles for the treatment of breast cancer which can be overcome with a system offering sensitive imaging and selective therapeutic effect. In this study, we developed a "dark-bright" multifunctional drug delivery system bringing real-time imaging and non-invasive therapy together. Theranostic ability of the system was delivered by Verteporfin (VP), serving as a fluorescence probe and a photosensitizer. To create a "dark state" system via self-quenching ability of VP, it was immobilized onto the superparamagnetic iron oxide nanoparticle (SPION) surface. Upon cellular uptake of the "dark state" system, release of VP led to fluorescence regain, switching the system to "bright state" after which photodynamic therapy (PDT) was initiated to lead to cell death. Theranostic feature of the system was evaluated in MCF-7 and MDA-MB-231 cell lines. Following internalization, fluorescence signal was increased up to ~56-fold in MCF-7 cells. The IC_{50} value decreased ~20-fold and ~117-fold in MCF-7 and MDA-MB-231 cell lines, respectively. Moreover, the system significantly inhibited migration in the highly aggressive MDA-MB-231 cell line and induced apoptosis by caspase-3 activation. The developed "dark-bright" system is a promising multifunctional drug delivery vehicle with extraordinary theranostic features for the detection and destruction of micro tumors.

1. Introduction

Breast cancer is the most common cancer in women with 2.3 million new cases resulting in approximately 700,000 deaths each year [1]. The first-line treatment modalities are surgery, radiotherapy, chemotherapy and hormone-based therapies [2]. Although current treatment protocols aid a substantial proportion of patients, particularly in aggressive cases these treatments are not successful due to leftover and/or resistant cell's ability to trigger recurrence and/or metastases of the disease[3]. Moreover, breast cancer's heterogeneous nature and high prevalence demonstrates the need for enhanced therapeutic strategies that both increase efficacy and minimize off-target effects. Hence, development of new methods with high sensitivity and enhanced selectivity to acquire precise detection and efficient treatment is crucial.

Starting from 2010, multi-functional systems called "theranostics" have emerged as exceptional platforms offering diagnosis and treatment concomitantly [4,5,6,7,8]. Cancer nano-theranostics possess the potential to address challenges associated with the management of heterogeneous and aggressive solid tumors [9,10]. Besides, targeting and controlled drug release can be accomplished by surface modification of theranostic nanoparticles making them attractive agent for cancer treatment [11,12,13]. Therefore, the number of studies investigating nanoparticle-based theranostic systems which combine multiple imaging techniques and/or treatment methods was tremendously amplified some of which were transferred to clinical studies [14,15,16–17,18,5,19,20,21]. Several clinical trials for local and/or metastatic breast cancer have been successfully completed and many other promising studies are still in progress (NCT01730833, NCT00662129, NCT00629499, NCT00110695, NCT00915369, NCT00609791). Despite the tremendous progress, the ability of theranostic systems to detect and destroy micro tumors is still limited causing residual and/or drug-resistant micrometastatic tumors to escape from diagnosis and treatment. Therefore, novel theranostic agents should be developed for precise diagnosis and effective treatment to remove

* Corresponding author.
E-mail address: serdem@medipol.edu.tr (S. Sibel Erdem).

https://doi.org/10.1016/j.ejpb.2025.114632
Received 26 August 2024; Received in revised form 7 January 2025; Accepted 10 January 2025
Available online 19 January 2025

residual and drug resistant micrometastatic tumors.

Among several nanoparticle-mediated theranostic systems, superparamagnetic iron oxide nanoparticles (SPION) are preferred due to their high surface/volume ratio, high specific absorption rate, and low toxicity [22]. The ease of modifying their surface with antibodies, aptamers, fluorescent agents, chemotherapeutic drugs and/or photodynamic therapy (PDT) agents makes SPION a favorable vehicle for theranostics.

PDT is a minimally invasive and local treatment method that uses visible or near-IR radiation to activate the photosensitizer to destroy malignant cells. Compared to conventional cancer therapies, PDT is advantageous due to its selectivity and short recovery time with minimum side effects [23,24]. Briefly, as the photosensitizer is activated by radiation, free radicals and/or singlet oxygen are generated, leading to apoptosis, necrosis or autophagy [25,26,27]. Besides, photosensitizers can serve as a fluorescent probe to visualize tumor tissue and to follow up the treatment [28,29]. Among several photosensitizers, FDA approved porphyrin derivative Verteporfin (VP) enables deep tissue penetration due to its strong absorption and emission (690 nm) in the visible region of the electromagnetic spectrum and its short circulation time (~5–6 h) offers a safe treatment with minor side effects [30,31,32].

Here we present a nanoscale "dark-bright" theranostic system composed of two major constituents: VP, serving as a fluorescence probe and photosensitizer, and SPION as a drug delivery vehicle. Proximity of VP molecules conjugated on the SPION surface results in fluorescence self-quenching and the system is designated as a "dark state". When the theranostic system is internalized by the target cell, VP molecules are released from the SPION surface through lysosomal cleavage yielding fluorescence signal recovery. As the fluorescence is restored the system shifts to "bright state". The "bright state" is a sign to initiate the treatment and imaging. The developed multifunctional "dark-bright" system offers sensitive dual imaging (fluorescence and MR imaging) and effective dual therapy (PDT, hyperthermia) for cancer (Fig. 1).

2. Materials and Methods

2.1. Materials

Unless otherwise stated, all reagents and disposables were purchased from commercial sources. VP (≥94 %), N-Hydroxysuccinimide (NHS), Thiazolyl blue tetrazolium bromide (98 %) (MTT) and Amicon ultra centrifugal filter (50 kDa) were purchased from Sigma Aldrich. Human breast cancer cell lines (MCF-7, MDA-MB-231) and mouse fibroblast cell line (NIH/3T3) were purchased from ATCC (American Type Culture Collection). N-ethyl-N'-(3-dimethylaminopropyl)-carboimide (EDC) was purchased from Acros. Dulbecco's Modified Eagle's Medium (DMEM) with high glucose, DMEM with high glucose/without phenol red, Fetal Bovine Serum (FBS), Bovine Calf Serum (BCS), Dulbecco's Phosphate Buffered Saline (DPBS) w/o Ca-Mg, DPBS w/Ca-Mg, Penicillin/Streptomycin Solution and 0.5 % Trypsin EDTA (10X) were purchased from Gibco. Bcl-2 (Rabbit mAB 4223), Bax (Rabbit mAb 5023) and β-actin (Rabbit mAb 4970S) were purchased from Cell Signaling Technology. HRP conjugated secondary antibody (Goat anti-rabbit IgG) and Hoechst 33258 (Pentahydrate (bis-Benzimide)) were purchased from Invitrogen. Calcein AM and Propidium Iodide (PI) were obtained from eBioscience and Genaxxon Bioscience, respectively. The caspase-3 activity was determined using Elabscience E-CK-A311 caspase-3 detection kit. Spectrophotometric analyses were performed on a microplate reader (Molecular Devices, Spectramax i3). Hydrodynamic size of the nanoparticles was measured using dynamic light scattering (DLS) (Zetasizer Nano-ZS, Malvern Instruments, Malvern, UK). As a light source for PDT, a 150 W QTH lamp equipped with a 610 nm long-pass filter and liquid light guide was used. A power meter, purchased from Newport, was used to measure the power of light. Confocal images were taken with 20x objectives on a Zeiss LSM800 confocal microscope (Carl Zeiss). Trans-Blot Turbo semi-dry transfer system, Mini-Protean Tetra vertical electrophoresis system and ChemiDoc gel documentation system were used for western blot analysis (Bio-Rad). Magnetic nanoparticles were analyzed with The JEOL JEM 2100 PLUS (200 kV LaB6) transmission electron microscope (TEM). X-ray diffraction (XRD) analyses were performed on Bruker D8 Advance and VSM analysis were conducted on a Lake Shore 7404 magnetometer.

2.2. Cell culture

MCF-7 cells were maintained in DMEM supplemented with 1 % penicillin/streptomycin (100 U/mL penicillin, 100 g/mL streptomycin), 0,1% insulin (0,01 mg/mL insulin) and 10 % FBS. MDA-MB-231 cells were cultured in DMEM supplemented with 1 % penicillin/streptomycin (100 U/mL penicillin, 100 g/mL streptomycin) and 10 % FBS. NIH/3T3 cells were cultured in DMEM supplemented with 1 % penicillin/streptomycin (100 U/mL penicillin, 100 g/mL streptomycin) and 10 % BCS.

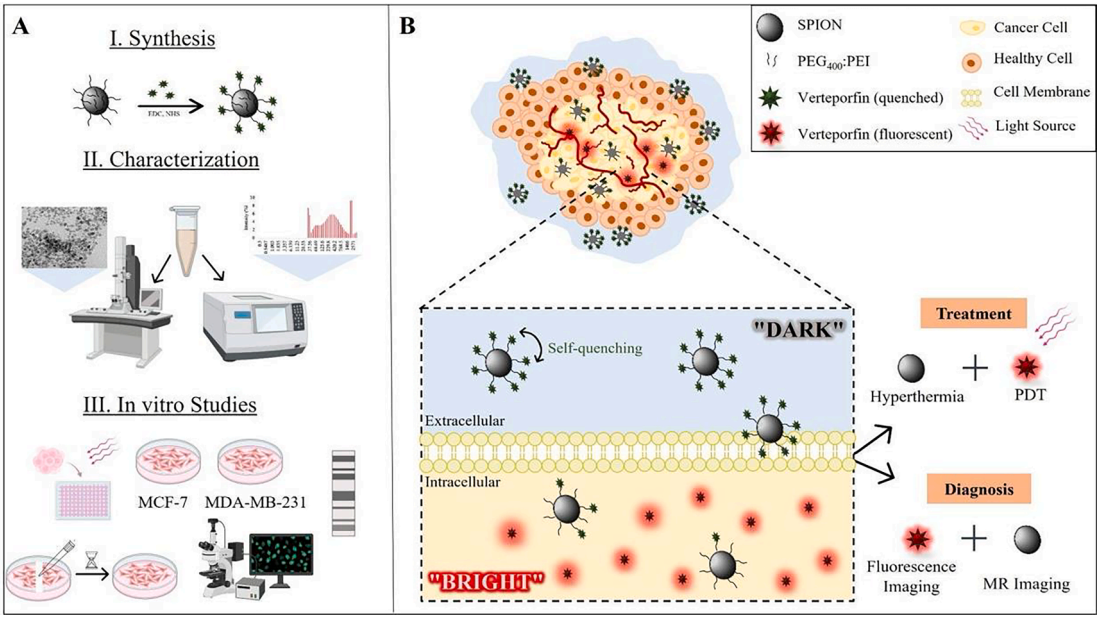

Fig. 1. A) Work flow of the designed study. **B)** Working principle of "dark-bright" system offering dual imaging and dual therapy.

All cells were incubated at 37 °C in a humidified atmosphere of 95 % / 5 % air/CO_2 and subcultured twice weekly.

2.3. Characterization of SPION

2.3.1. Transmission electron microscopy (TEM)

The size and morphology of the magnetic nanoparticles synthesized via the coprecipitation method [33] were analysed using a TEM. The aqueous nanofluids were dropped onto 200 mesh copper TEM grids and allowed to dry under ambient conditions. The mean size and size distribution of the nanoparticles were subsequently obtained by measuring the long and short axes of 100 different nanoparticles in TEM images using ImageJ.

2.3.2. X-ray diffraction (XRD)

The crystal structure and phase identification of the synthesized magnetic nanoparticles were determined through XRD. Analyses were conducted at room temperature, with scans performed within the range of 20–70 2θ on powder form samples. Subsequently, phase determination was carried out by comparing the positions and relative intensity ratios of the peaks present in the obtained diffraction patterns with those of reference patterns.

2.3.3. Vibrating sample magnetometer (VSM)

A vibrating sample magnetometer (VSM) was utilized to determine the magnetic properties of the synthesized magnetite nanoparticles. The corresponding measurements were conducted at room temperature within the range of ± 20 kOe field intensity using the samples in powder form and the magnetic behavior and saturation magnetization of the samples were subsequently determined.

2.4. Surface modification of SPION with Verteporfin

SPION (1.00:0.66:0.66; Fe:PEG_{400}:PEI) was synthesized as detailed in our recent publication [33]. The surface of the SPION (1 mL, 600 μgFe/mL) was modified with 100 nmol VP. VP:EDC:NHS in 1:7.5:3.15 mol ratios were dissolved in ~ 100 μL 10 % DMSO (aq) solution. The pH of the solution was brought up to 8–9 using 1 M Triethylamine and the reaction mixture was left overnight at 37℃. The centrifugal filtration (50 kDa Amicon Ultra Filter) at 3500 rpm for 5 min at 4℃ was performed twice. VP and SPION concentrations in the theranostic system were spectroscopically determined employing Beer-Lambert Law at 690 and 305 nm. Hydrodynamic size and zeta potential of the VP-SPION were measured using DLS at a 173° scattering angle with a 4-mW He–Ne laser at room temperature.

2.5. Assessment of fluorescence quenching of the theranostic system

Three groups were used to evaluate the fluorescence quenching of the system: i) VP-SPION, ii) VP and iii) SPION + VP (mixture). Each group had 500 nM VP in 1 % DMSO solution in phenol red free medium. Fluorescence spectrum of each solution was recorded at 465–750 nm (ex. at 440 nm) with 5 nm intervals. Quenching factors (QF1 and QF2) were calculated using the formulas below:

QF1 = Fluorescence Intensity of Mixture/Fluorescence Intensity of VP-SPION

QF2 = Fluorescence Intensity of VP/ Fluorescence Intensity of VP-SPION

2.6. Determination of hemolytic activity

For the assessment of hemolytic activity against SPION and VP-SPION, the hemolysis assay was conducted by modifying the method described by Chen et al. [34]. Briefly, a 5 mL full blood sample that is derived from three different volunteers centrifuged at 3500 rpm for 5 min. Red blood cells (RBCs) were washed three times with PBS (pH 7.4) and diluted with PBS in 1:10 vol ratio. The diluted RBCs were incubated with SPION and VP-SPION with final concentrations ranging from 0.5 μgFe/mL to 100 μgFe/mL at 37 °C for 1 h. Triton X-100 (1 % v/v) and RBCs in PBS were used as positive control and negative control, respectively. After the incubation period, the samples were centrifuged at 14,800 rpm for 30 min to remove RBCs from the solution. The absorption of supernatants was measured at 541 nm using a microplate reader.

The percentage of hemolysis was calculated according to the following equation:

$$\text{Hemolysis \%} = (\text{Test well} - \text{Negative Control} / \text{Positive Control} - \text{Negative Control}) \times 100$$

2.7. Assessment of cellular internalization of the theranostic system

100,000 NIH/3T3 and 200,000 MCF-7 cells in 1.5 mL DMEM were seeded into 35 mm glass-bottom petri dishes and allowed to adhere for 24 h. The cells were incubated with 500 nM VP and equimolar amounts of VP containing SPION conjugate for 0, 6 and 24 h. Intracellular fluorescence intensity at 0 h was compared to fluorescence intensity at each time period to determine the optimum incubation time to initiate PDT. The cells were stained with Hoechst 33258 and images were captured using appropriate filters for Hoechst (ex/em: 352/461 nm) and VP (ex/em: 488/590 nm).

2.8. Cytotoxicity assay

Toxicity of VP, SPION, and VP-SPION towards selected cell lines were investigated using MTT assay. 7,000 NIH/3T3, 15,000 MCF-7 and 7,000 MDA-MB-231 cells per well were seeded into a 96-well plate and allowed to adhere for 24 h. The cells were separately incubated with 75–1200 nM VP, 0.5–100 μgFe/mL SPION, and VP-SPION having 75–1200 nM VP. Following 24 h of incubation, 5 μL MTT solution (5 mg/mL in PBS) was added to each well and incubated for 3 h. The cell culture medium was discarded and the formazan products were dissolved in 200 μL DMSO. The optical density was measured at 570 nm. The relative cell viability (%) was normalized with the untreated (100 % viable) and Tween-20 treated (0 % viable) control groups.

2.9. Phototoxicity assay

MCF-7, MDA-MB-231 and NIH/3T3 cells were prepared as described in the cytotoxicity assay. The cells were separately incubated with 75–1200 nM VP and 75–1200 nM VP containing SPION conjugates. After 24 h of incubation, the medium was replaced with 100 μL fresh medium. The cells were exposed to 20 J/cm^2 light dose and incubated for 24 h at 37 °C. Cell viability was determined with MTT assay as detailed in the cytotoxicity assay.

2.10. Assessment of cell viability

100,000 NIH/3T3, 200,000 MCF-7 and 250,000 MDA-MB-231 cells were seeded into 35 mm glass-bottomed petri dishes and placed into the CO_2 incubator for 24 h. The cells were treated with VP and VP-SPION at the IC_{50} values for 24 h at 37 °C. PDT was carried out as described in the phototoxicity assay. After 24 h, the cells were incubated with 1 μl Calcein AM (3 mg/mL in DMSO) and 1 μL PI (1 mg/mL in dH_2O) at room temperature for 10 min. Cell images were captured using appropriate filters for Calcein AM (ex/em: 496/516 nm) and PI (ex/em: 482/608 nm). Untreated and 0.05 % Tween 20 treated cells were included as positive and negative control groups, respectively. The live/dead ratio was calculated based on the cell numbers in each group and normalized to the viable cell number of the positive control group.

2.11. Scratch assay

MCF-7 and MDA-MB-231 cells (400,000/petri dish) were cultured in 35 mm petri dishes and allowed to reach 80 % confluency. Using a sterile 200 μL micropipette tip, a cell layer was scraped to generate a 1 mm width cell-free area and the wound images (0 h) were taken using an inverted light microscope. The cells were incubated with VP and VP-SPION at the IC_{50} values for 24 h. PDT was carried out as described in the phototoxicity assay and the cells were allowed to migrate for 24 h. Upon the completion of migration, the wound images were re-taken from the same regions. All images were acquired in triplicate by using an inverted light microscope at 5x objective. Gap size was analyzed using Image-J software and the percentage of wound closure was determined for each group comparing the gap sizes before and after treatments. One-way ANOVA analysis was performed using GraphPad Prism and $p < 0.05$ was considered as statistically significant.

2.12. Western blotting

250,000 MCF-7 cells were seeded to 35 mm petri dishes and incubated with VP and VP-SPION at the IC_{50} values for 24 h. Following the incubation, PDT was performed as described in the phototoxicity assay. Following 24 h incubation, western blot analysis was conducted. Briefly, cell lysates were prepared using the RIPA buffer to extract total protein, subsequently an equal amount of protein (20 μg) from each lysate was loaded into the wells to perform gel electrophoresis. Proteins were transferred to PVDF membranes by semi-dry transfer. Membranes were blocked using 5 % non-fat milk in 50 mmol Tris-buffered saline containing 0.1 % Tween (TBS-T; blocking solution) for an hour at room temperature. The membranes were incubated with 1:2000 diluted β-actin, Bax or Bcl-2 antibodies at 2–8 °C overnight. Following the incubation, HRP-conjugated secondary antibodies were introduced to the membranes for 1 h at room temperature. Bax and Bcl-2 protein bands were visualized using Enhanced Chemiluminescence (ECL) method. Image J software was used for the quantitative analysis and data were normalized to β-actin. One-way ANOVA analysis was performed using GraphPad Prism and $p < 0.05$ was considered as statistically significant.

2.13. Caspase-3 activity determination

MCF-7 and MDA-MB-231 cells (750,000 cells/petri dish) were cultured in 35 mm petri dishes and placed into the CO_2 incubator for 24 h. The cells were incubated with VP and VP-SPION at the IC_{50} values for 24 h. PDT was carried out as described in the phototoxicity assay. An additional untreated group was included as a control (100 % viable). After 3 h, following the manufacturer's instructions the cell lysates were prepared [33]. Cell lysates, having 150 μg protein in each well, were loaded into a 96-well plate incubated at 37 °C overnight. The experiment was performed in triplicate for each group. Optical densities were measured at 405 nm and caspase-3 activity was determined using a colorimetric caspase-3 detection kit. The results were expressed as the fold change relative to the control group. One-way ANOVA analysis was performed using GraphPad Prism and $p < 0.05$ was considered as statistically significant.

The caspase activity of each group was calculated using the following formula:

$$(OD_{sample} - OD_{blank})/(OD_{negative}\text{control} - OD_{blank})$$

3. Results

A morphological and dimensional analysis of the nanoparticles synthesized by the co-precipitation method was carried out using TEM. The results demonstrated that the majority of the nanoparticles exhibited irregular morphologies along with spherical or cubic structures **(**Fig. 2**A).** Furthermore, the mean size of the particles was determined to be 8.0 ± 1.4 nm, based on data obtained from the measurements taken on the long and short axes of individual particles (Fig. 2**B**). The relatively smaller average size, in conjunction with the narrow size distribution of the nanoparticles obtained via the co-precipitation method, suggests that nucleation plays a more dominant role during formation than the growth phase**.** In addition, XRD was employed to identify the phase of the synthesized nanoparticles by revealing crystal structure and the results indicated that 2θ values and corresponding intensity ratios of all peaks matched with those of the [220], [311], [400], [511] and [440] planes of magnetite (**Fig. S1**). Finally, the magnetisation curves obtained by VSM demonstrated that the nanoparticles possessed a saturation magnetization of 51.8 emu/g and the absence of coercivity and a residual magnetisation following the removal of external magnetic field indicated that the nanoparticles exhibited superparamagnetic properties (**Fig. S2**).

The magnetite nanoparticles were coated with PEG_{400}:PEI for surface modification [33] after which the theranostic system was constructed simply by immobilizing VP onto the SPION surface. SPION recovery and yield of VP conjugation were 83 % and 46 %, respectively. Fe_3O_4 and VP concentrations were determined as 497 μgFe/mL and 41 μM,

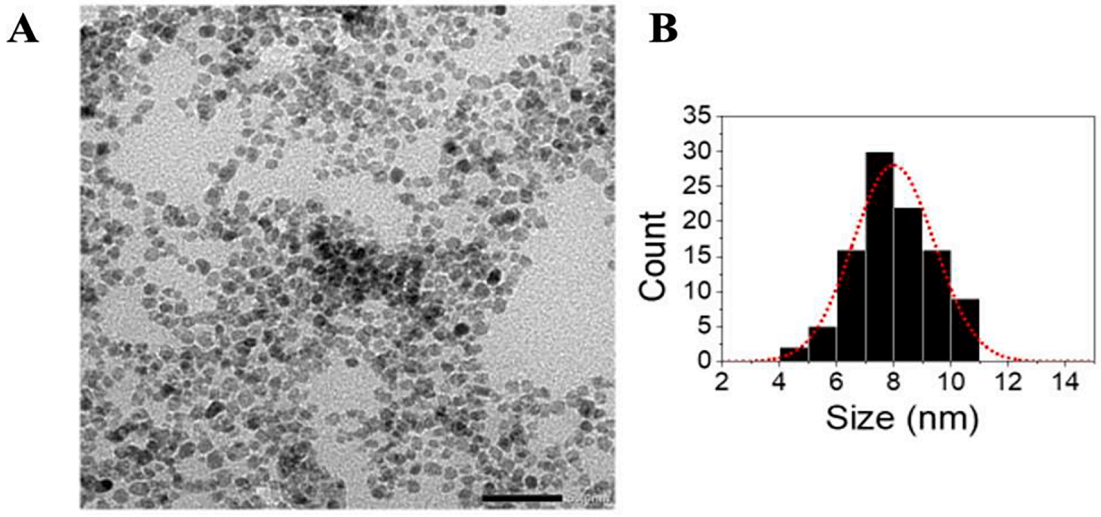

Fig. 2. A) TEM image of magnetite nanoparticles synthesized via co-precipitation method and **B)** corresponding size distribution of nanoparticles. (Scale bar = 50 nm.).

respectively (Table S1). The surface charge of SPION was 13 ± 0.61 mV while the VP-SPION's was 31 ± 1.35 mV. The size of SPION and VP-SPION were determined as 158.8 ± 2.2 nm and 218.5 ± 6.39 nm, respectively (Fig. S3,4).

To show proof of concept of the "dark-bright" system, QF of the VP-SPION was evaluated by fluorescence-based assay. Fluorescence spectra of VP, VP-SPION and mixture (to mimic "bright state") were acquired and fluorescence intensity at 695 nm was used to assess QFs (Fig. 3). Comparison of fluorescence intensity of mixture ("bright state") to VP-SPION ("dark state") revealed that at least ~ 16-fold fluorescence quenching was achieved with the "dark state" system (**QF1,** Table S3). When emission maxima of VP-SPION ("dark state") was compared to equimolar concentration of VP solution, ~18-fold QF was obtained (**QF2,** Table S3). The fluorescence recovery of the system was determined as ~ 91 % by simply taking ratio of fluorescence intensities of the mixture ("bright state") and VP (Table S3).

The hemocompatibility of the developed theranostic agent was evaluated with hemolysis assay. Human RBCs were treated with SPION and VP-SPION with different concentrations (Fig. 4). The hemolytic activity level of the SPION and VP-SPION were less than 5 % up to concentration of 15 μgFe/mL. Hemolytic damage was pronounced above 70 μgFe/mL concentration for SPION and VP-SPION which is well above the applied concentration throughout the study.

The developed system was subjected to further investigation to examine cellular uptake by confocal microscopy. Intracellular fluorescence intensity gradually increased and reached its maximum value within 24 h for VP and VP-SPION in the selected cell lines (Fig. 5). While internalization of VP by MCF-7 cells yielded ~ 35-fold increase in fluorescence signal, VP-SPION internalization resulted in ~ 56-fold increase in fluorescence intensity. On the other hand, when the experiment was conducted in NIH/3T3 control cell line, only a slight fluorescence increase was detected with VP and VP-SPION (Table S4,5).

Cytotoxicity of the SPION on the selected cell lines was evaluated (Fig. 6). The results verified that cell viability remained as high as 75 % at concentrations of ≤ 10 μgFe/mL SPION. The IC_{50} values of SPION were calculated as 18.8, 13.5 and 27.2 μgFe/mL for NIH/3T3, MCF-7 and MDA-MB-231 cell lines, respectively (Fig. S5).

The cytotoxicity analysis of VP and VP-SPION revealed that the agents had negligible toxicity on the selected cell lines up to 900 nM VP concentration in the absence of light (Fig. 7, Fig. S6). Following PDT, a concentration-dependent toxicity was observed in MCF-7 and MDA-MB-231 cell lines for both VP and VP-SPION (Fig. 7). While conjugation of VP onto the SPION surface decreased IC_{50} value almost twice as much from 582 nM to 294 nM in MCF-7 cells, it decreased IC_{50} concentration from 60 nM to 48 nM in MDA-MB-231 cell line (Fig. S7). Neither VP nor VP-SPION showed any toxicity towards the NIH/3T3 cell line.

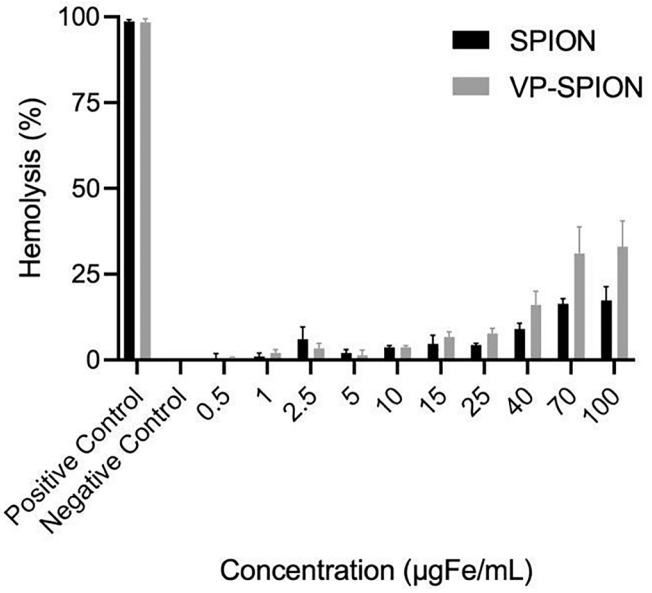

Fig. 4. The hemolytic activity level of the SPION and VP-SPION.

Phototoxicity was further elaborated using a two-color fluorescence assay. The results showed that 37 % and 33 % cell death was achieved when the cells were incubated with VP-SPION at IC_{50} concentration in MCF-7 and MDA-MB-231 cell lines, respectively. On the other hand, when an equimolar concentration of VP was used for the treatment, only 14 % and 23 % cell death were achieved for the MCF-7 and MDA-MB31 cell lines, respectively. NIH/3T3 cell line retained 100 % viability under the identical conditions (Fig. 8).

The migration ability of the MCF-7 and MDA-MB-231 cells in response to PDT was evaluated using scratch assay. The cell images, captured before and after the PDT, were shown in Fig. 9**A,C.** The gap closures were calculated as 4 %, 6 % and 27 % in VP-SPION, VP and

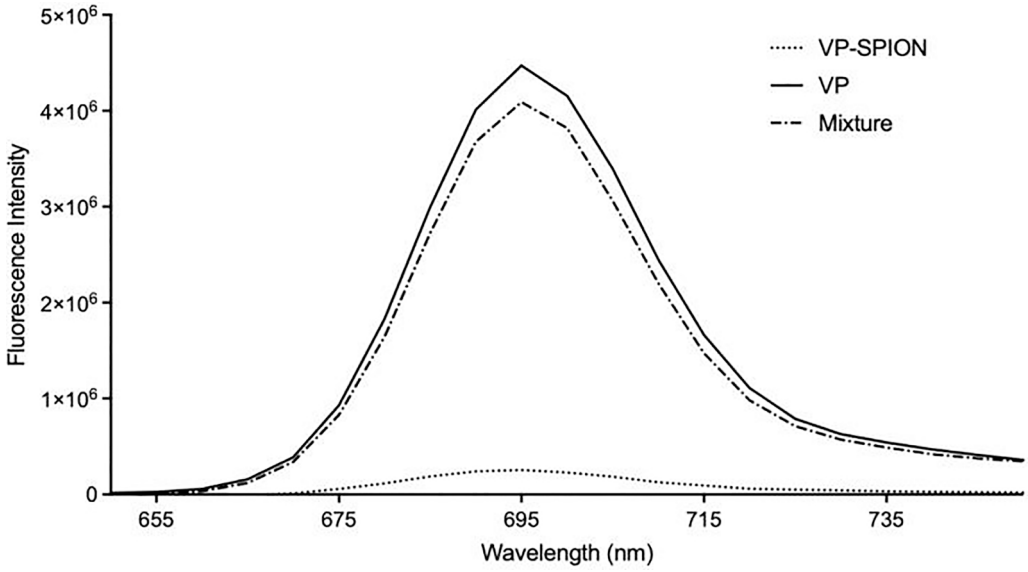

Fig. 3. Fluorescence spectra of "VP", "mixture" and "VP- SPION" in 1 % DMSO in phenol red free medium. Excitation wavelength is 440 nm. (For interpretation of the references to color in this figure legend, the reader is referred to the web version of this article.)

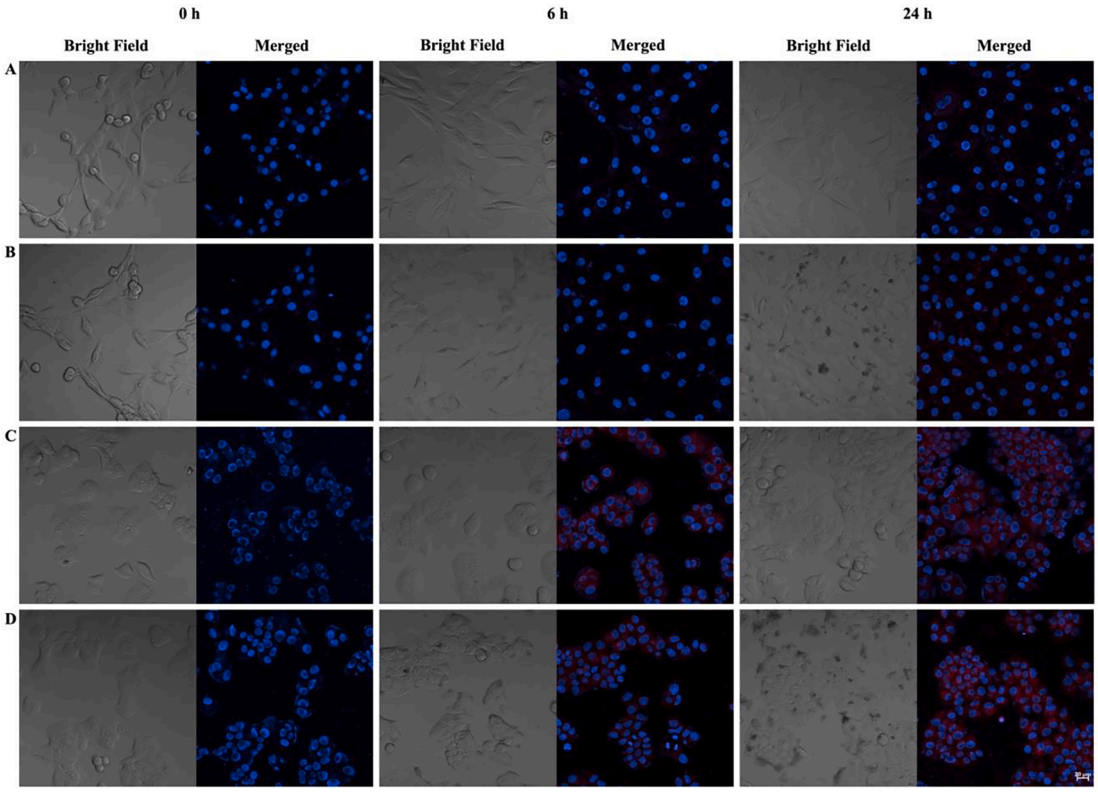

Fig. 5. Confocal images of **A)** NIH/3T3 cells treated with VP, **A)** NIH/3T3 cells treated with VP-SPION, **C)** MCF-7 cells treated with VP and **D)** MCF-7 cells treated with VP-SPION at different time intervals (0 h, 6 h and 24 h).

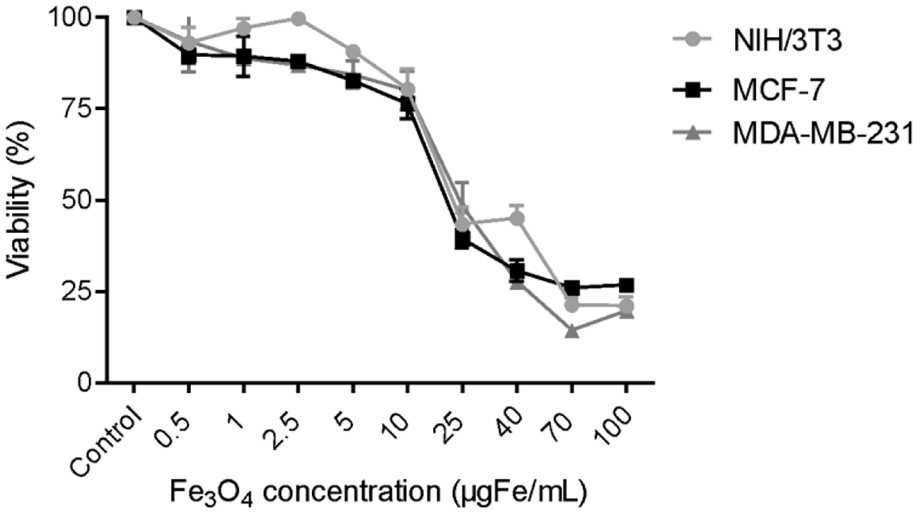

Fig. 6. Cytotoxicity of SPION towards NIH/3T3, MCF-7 and MDA-MB-231 cell lines.

control groups in MCF-7 cell line, respectively (Fig. 9**B**). These findings indicate that both agents had a similar impact on the rate of cell migration, yet both varied considerably from the control group ($p < 0.05$). However, the difference between the VP and VP-SPION treatment groups was not statistically significant (Fig. 9**B**). For highly aggressive MDA-MB-231 cell line, the gap area decreased up to 30 %, 88 % and 94 % in VP-SPION, VP and control groups, respectively (Fig. 9**D**). While exposure of both VP and VP-SPION significantly reduced the migration ability of MDA-MB-231, VP-SPION resulted in statistically stronger inhibition compared to VP only treatment (Fig. 9**D**).

A western blot analysis was conducted to examine the effect of PDT on Bax and Bcl-2 protein expression levels. The protein band intensities of β-Actin, Bax, and Bcl-2 were detected at 45 kDa, 26 kDa, and 20 kDa, respectively (Fig. 10**A**). According to the one-way ANOVA analysis, Bax/

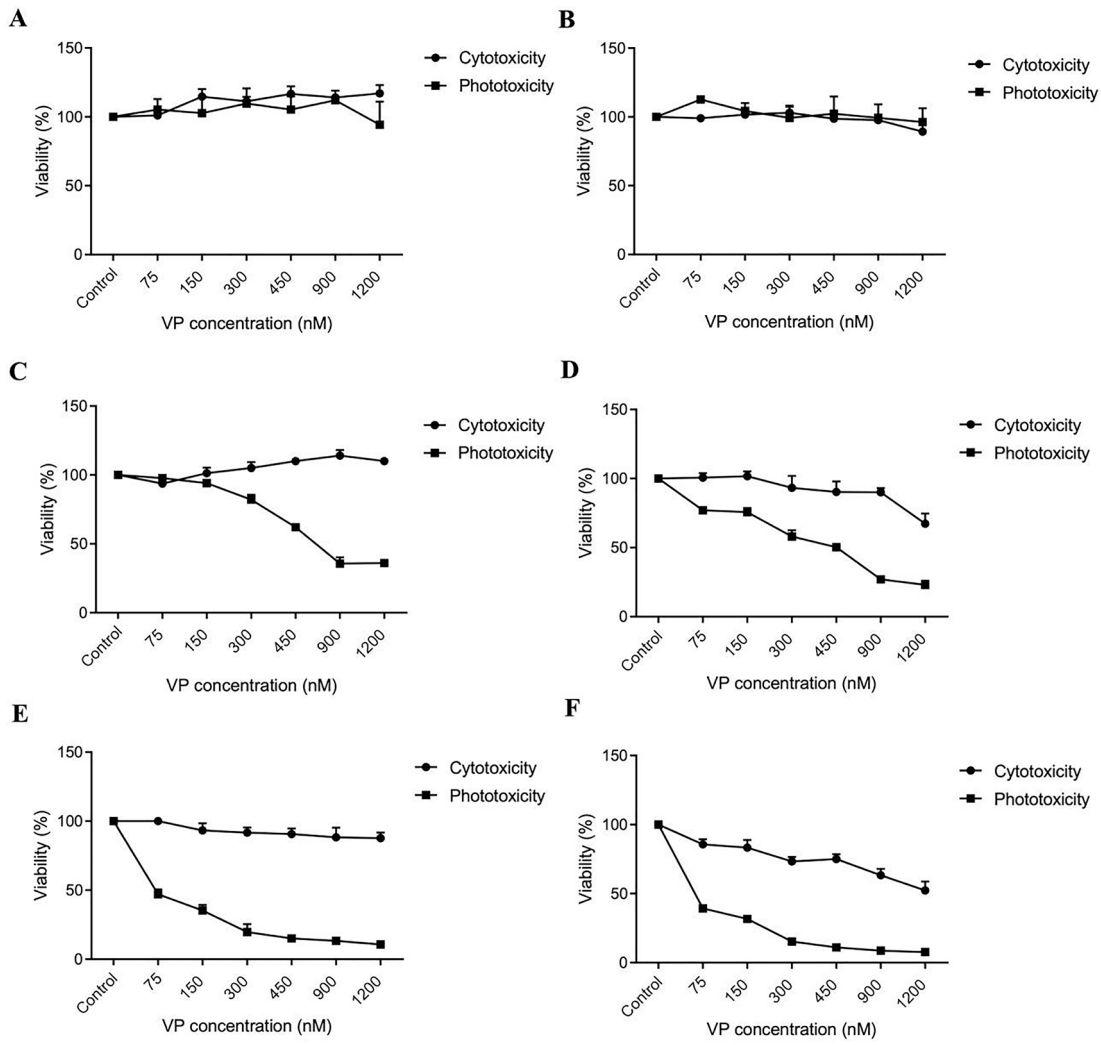

Fig. 7. Toxicity analysis of VP towards **A)** NIH/3T3, **C)** MCF-7 and **E)** MDA-MB-231, respectively. Toxicity analysis of VP-SPION towards **B)** NIH/3T3, **D)** MCF-7 and **F)** MDA-MB-231, respectively.

Bcl-2 ratios were significantly increased following VP and VP-SPION treatment compared to the control group. Notably, the increase in Bax/Bcl-2 ratio in VP-SPION treated cells was statistically more significant than VP treated cells (Fig. 10**B**).

The caspase-3 assay was conducted to evaluate the effects of VP and VP-SPION treatments on the induction of apoptosis in the selected cell lines. The results showed that VP treatment resulted in 2.9 and 1.7- fold increase in MCF-7 and MDA-MB-231 cells, respectively. Moreover, the increase in caspase-3 activity was more pronounced in response to VP-SPION treatment, showing 3.5 and 2.8- fold in MCF-7 and MDA-MB-231 cells, respectively. Statistical analysis revealed a high level of significance ($p < 0.0001$) for all treatment groups in both cell lines (Fig. 11).

4. Discussion

SPION (1.00:0.66:0.66; Fe:PEG_{400}:PEI) was synthesized using the protocol described in our previous publication [33]. *In vitro* studies revealed that the toxicity of the SPION was considerably low at the concentration $\leq$ 10 μgFe/mL. Accordingly, Fe_3O_4 concentration was kept below 10 μgFe/mL throughout the study to avoid the toxicity of the SPION (Fig. 6).

Conjugation of VP to SPION surface allowed the construction of a potent nano-scale theranostic system delivering enhanced fluorescence imaging and effective treatment. VP was immobilized onto the SPION surface with almost 50 % efficiency without significant SPION loss (**Table S1**). VP concentration in the theranostic system is a principal parameter for the efficacy of the "dark-bright" system. As the amount of VP increases, proximity of VP molecules on the SPION decreases, yielding fluorescence quenching of the system. Having a "dark state" system is vital to eliminate background and off-target fluorescence signal for *in vivo* applications. Besides, as the system is internalized by the target cell, the amount of VP released from SPION is directly proportional to the fluorescence regain and to the therapeutic efficacy of the system.

To assess the effectiveness of the "dark-bright" system, fluorescence intensities of VP, VP-SPION and mixture at equimolar concentrations were determined spectroscopically. As the system switched from the "dark state" to "bright state" the fluorescence intensity increased up to ~ 16-fold (QF1). Furthermore, the fluorescence intensity would increase

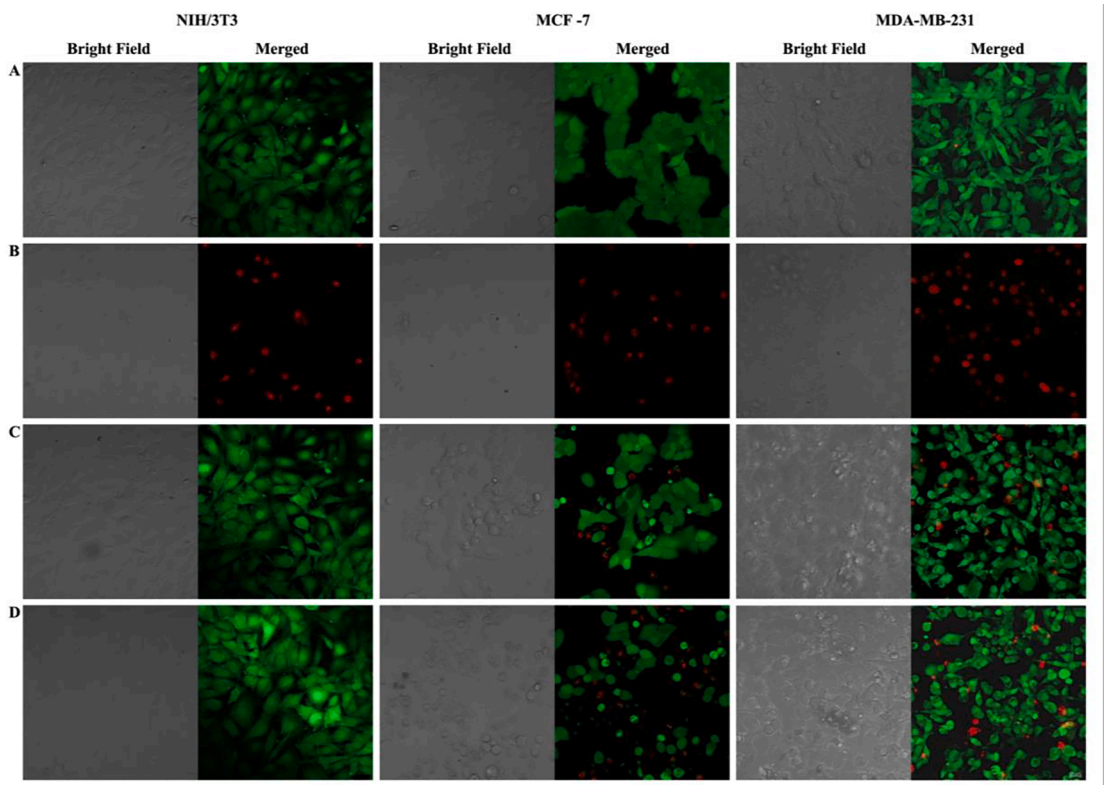

Fig. 8. Confocal images of NIH/3T3, MCF-7 and MDA-MB-231 cells **A)** Untreated (positive control), **B)** Tween20 (negative control), **C)** VP treatment **D)** VP-SPION treatment groups.

up to ~ 18-fold if VP is completely released from the SPION surface (QF2). Consequently, achievement of high fluorescence recovery (~ 91 %) was the initial evidence for an exceptional imaging capability of the developed theranostic system (**Table S3**).

Hemocompatibility of SPION and VP-SPION was analyzed by hemolysis assay. SPION and VP-SPION showed negligible hemolytic activity below < 15 μgFe/mL, indicating its potential for *in vivo* studies (Fig. 4).

The internalization of the system was examined to determine the optimal incubation time to initiate PDT. The confocal microscopy images confirmed that the highest intracellular concentration of the theranostic system was achieved within 24 h in the selected cell lines. Uptake of VP-SPION by MCF-7 and NIH/3T3 cells resulted in ~ 56-fold and ~ 15-fold fluorescence amplification, respectively indicating VP-SPION was internalized by cancer cells ~ 4 times more than the control cells (**Table S4,5**). Based on the results, ideal incubation time to perform PDT was defined as 24 h.

It is vital that the theranostic agent maintains "dark state" up until VP's release on site to eliminate any possible adverse effects. *In vitro* viability studies showed that neither VP nor VP-SPION treatments caused significant toxicity in the absence of light (Fig. 8). Following activation of the VP via PDT, while VP and VP-SPION did not show any toxicity towards the NIH/3T3 cell line, significant toxicity was observed in the MDA-MB-231 and MCF-7 cell lines. Roughly 20-fold less VP-SPION was required to achieve 50 % cell death in MCF-7 cell line compared to control group, whereas the VP-SPION concentration was decreased approximately 117-fold in the more aggressive MDA-MB-231 cell line to obtain equal phototoxic effect (**Fig. S7**). The findings indicate that the theranostic agent accumulates more efficiently in breast cancer cell lines compared to healthy fibroblastic cells. Besides, comparison of VP with VP-SPION confirmed that when VP immobilized onto the SPION surface, it caused nearly 50 % and 20 % more cell death in MCF-7 and MDA-MB-231 cell line, respectively (**Fig. S7**). Further analysis of cell viability was conducted by two-color fluorescence assay and the results were comparable to the phototoxicity assay (Fig. 8). In the light of these results, we speculate that the accumulation of the theranostic agent in much higher concentration in cancer cells suggests that it'd be a promising agent for passive targeting of cancer.

Magnitude of PDT on cellular migration was also studied in MCF-7 and MDA-MB-231 cell lines by employing scratch assay. Migration was triggered with the introduction of a scratch, and the captured images revealed that treatment with VP inhibited cell migration in both MCF-7 and MDA-MB-231 breast cancer cell lines to various degrees. On the other hand, suppression of migration was statistically more significant predominantly in the more aggressive cell line compared to the VP only treatment (Fig. 9**D**). As it was highlighted in the literature, genomic differences between two breast cancer cell lines can alter their migratory capacity ([35,36]). Even though MDA-MB-231 cells are known to exhibit a higher migratory potential compared to MCF-7 cells [37], our results shows that VP-SPION had higher potency on inhibition of migration in the aggressive cell line. The enhanced efficacy of the developed theranostic agent in the MDA-MB-231 cells suggests that it may be particularly effective against triple-negative breast cancers, which are often associated with poor prognosis and treatment resistance. Our results show that the developed theranostic agent can be further advanced for targeted drug delivery strategies for different breast cancer subtypes.

PDT-induced apoptotic response of MCF-7 cells was investigated by

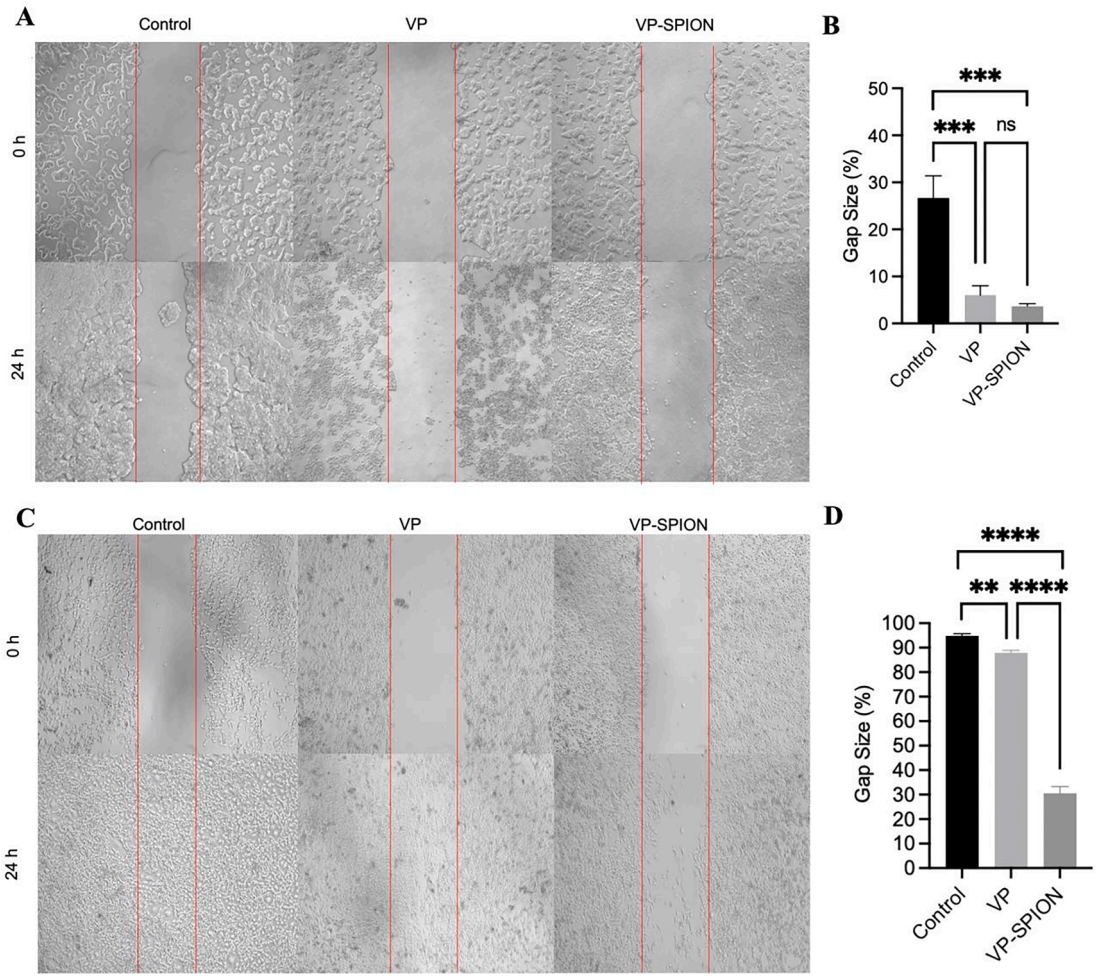

Fig. 9. Time-lapse (0–24 h) microscopy images of scratch assay towards **A)** MCF-7 and **C)** MDA-MB-231 cell lines. Statistical analysis of closure percentages over time **B)** MCF-7 and **D)** MDA-MB-231 cell lines, ***p < 0.001. (VP: Verteporfin, VP-SPION: Verteporfin SPION conjugate).

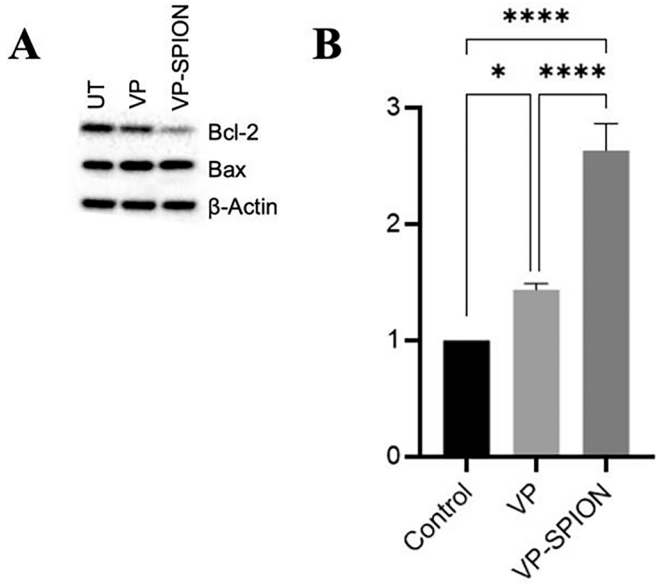

Fig. 10. Bax and Bcl-2 protein band intensities through western blot analysis. The comparison of Bax/Bcl-2 ratio levels in VP and VP-SPION-treated MCF-7 cells with the untreated group, *p < 0.05, ****p < 0.0001. (VP: Verteporfin, VP-SPION: Verteporfin SPION conjugate).

western blot analysis. Bax/Bcl-2 ratio is a widely used indicator to interpret pro-apoptotic and anti-apoptotic protein balance in cells [38]. Consequently, following photoactivation, we found a significant increase in the Bax/Bcl-2 ratio of VP and VP-SPION treated cells compared to the control group (Fig. 10**B**). VP-SPION exhibited a more predominant effect on Bax/Bcl-2 ratio than VP, confirming VP-SPION's ability to induce apoptosis. The observed increase in the Bax/Bcl-2 ratio in MCF-7 cells promote the activation of caspases, particularly caspase-3, which plays a vital role in mediating the apoptotic process [39,40] It is shown that as Bax/Bcl-2 ratio increases, sensitivity towards chemotherapy treatment decreases [41]. Therefore, development of new and/or adjuvant therapy options are essential to address these challenges. The upregulation of Bax/Bcl-2 ratio and increased phototoxicity due to VP-SPION treatment suggest that this system may serve as an alternative treatment option for standard chemotherapeutic modalities.

Increase in Bax/Bcl-2 ratio and induction of apoptosis was further supported with caspase-3 activity assay. Our results revealed that caspase-3 activation was significant in MCF-7 and MDA-MB-231 cell lines following VP and VP-SPION treatments. A more pronounced increase in both cell lines after VP-SPION treatment demonstrated the efficacy of the developed theranostic agent in inducing apoptosis even in highly aggressive breast cancer cells (Fig. 11). All these findings reveal that VP-SPION is an outstanding candidate that could be further investigated as a theranostic agent for microtumors.

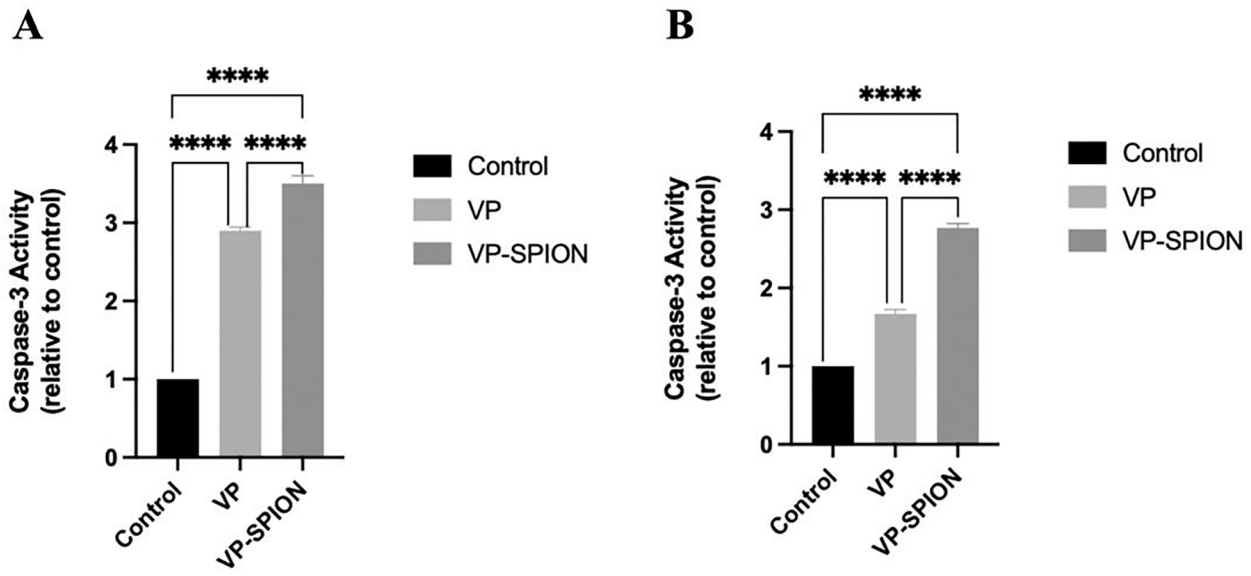

Fig. 11. Relative caspase activity in A) MCF-7 and B) MDA-MB-231 cell lines following VP and VP-SPION treatments compared to the control group ****$p < 0.0001$. VP: Verteporfin, VP-SPION: Verteporfin SPION conjugate).

5. Conclusion

In conclusion, a nanoscale theranostic system offering non-invasive localized treatment and sensitive fluorescence imaging with favorable QF (~ 18-fold) was developed. Decoration of the SPION surface with an adequate amount of VP maintained the system's "dark state" due to self-quenching of VP's fluorescence. Following internalization of the system in MCF-7 cells, VP was released and ~ 56-fold increase in fluorescence signal was achieved facilitating high tumor-to-background signaling for precise imaging. To the best of our knowledge, this is the first "dark-bright" theranostic system with the highest fluorescence recovery rate *in vitro*. Furthermore, the system showed high selectivity towards the selected cancer cell lines with varying levels of aggressiveness which is vital for imaging and treatment of microtumors. Besides, VP-SPION with ~ 20-fold and ~ 117-fold lower IC_{50} concentration in MCF-7 and MDA-MB-231 cell lines, respectively, compared to the control group proved that the system has not only superior diagnostic capability but also has an exceptional therapeutic effect. Additionally, the activated system inhibited cell migration and induced apoptosis by increasing the Bax/Bcl-2 ratio in MCF-7 cell line. The developed theranostic system demonstrated enhanced tumor-to-background signal ratio, high local phototoxicity, increased migration inhibition in both high and less aggressive breast cancer cell lines verifying its potential for further development such as a targeted nanoparticle platform.

Ethical Issues

İstanbul Medipol University Non-Invasive Clinical Reseacrh Ethical Committee with issue number E-10840098-202.3.02-7464.

CRediT authorship contribution statement

S. İrem Güler: Writing – review & editing, Writing – original draft, Validation, Investigation, Formal analysis. **Cem Levent Altan:** Validation, Methodology, Formal analysis, Conceptualization, Data curation, Supervision, Writing – review & editing. **E. Esma Demircioglu:** Data curation, Formal analysis, Validation, Writing – review & editing. **Nihan Verimli:** Writing – original draft, Formal analysis. **Beyza Abisoglu:** Methodology, Investigation, Formal analysis. **Cigdem Bayraktaroglu:** Investigation, Formal analysis. **Mustafa Caglar Beker:** Investigation, Formal analysis. **S. Sibel Erdem:** Writing – review & editing, Writing – original draft, Visualization, Validation, Supervision, Resources, Project administration, Methodology, Investigation, Funding acquisition, Formal analysis, Data curation, Conceptualization.

Declaration of competing interest

The authors declare that they have no known competing financial interests or personal relationships that could have appeared to influence the work reported in this paper.

Acknowledgment

The study described in this paper was supported by a grant from the Scientific and Technological Research Council of Turkey, TÜBİTAK with grant number 118S299.

Appendix A. Supplementary data

Supplementary data to this article can be found online at https://doi.org/10.1016/j.ejpb.2025.114632.

Data availability

Data will be made available on request.

References

[1] H. Sung, J. Ferlay, R.L. Siegel, M. Laversanne, I. Soerjomataram, A. Jemal, F. Bray, Global Cancer Statistics 2020: GLOBOCAN Estimates of Incidence and Mortality Worldwide for 36 Cancers in 185 Countries, CA Cancer J. Clin 71 (2021) 209–249, https://doi.org/10.3322/caac.21660.
[2] D. Radice, A. Redaelli, Breast cancer management: quality-of-life and cost considerations, Pharmacoeconomics 21 (2003) 383–396, https://doi.org/10.2165/00019053-200321060-00003.
[3] H.G. Welch, P.C. Prorok, A.J. O'Malley, B.S. Kramer, Breast-cancer tumor size, overdiagnosis, and mammography screening effectiveness, N. Engl. J. Med 375 (2016) 1438–1447, https://doi.org/10.1056/NEJMoa1600249.
[4] J.H. Choi, Y.J. Lee, D. Kim, Image-guided nanomedicine for cancer, J. Pharm. Investig 47 (2017) 51–64, https://doi.org/10.1007/s40005-016-0297-1.
[5] G.G. Genchi, A. Marino, C. Tapeinos, G. Ciofani, Smart Materials Meet Multifunctional Biomedical Devices: Current and Prospective Implications for Nanomedicine, Front. Bioeng. Biotechnol 5 (2017) 80, https://doi.org/10.3389/fbioe.2017.00080.
[6] P. Huang, J. Lin, S. Wang, Z. Zhou, Z. Li, Z. Wang, C. Zhang, X. Yue, G. Niu, M. Yang, D. Cui, X. Chen, Photosensitizer-conjugated silica-coated gold

nanoclusters for fluorescence imaging-guided photodynamic therapy, Biomaterials 34 (2013) 4643–4654, https://doi.org/10.1016/j.biomaterials.2013.02.063.
[7] L.B. Josefsen, R.W. Boyle, Unique diagnostic and therapeutic roles of porphyrins and phthalocyanines in photodynamic therapy, imaging and theranostics, Theranostics 2 (2012) 916–966, https://doi.org/10.7150/thno.4571.
[8] O. Taratula, C. Schumann, M.A. Naleway, A.J. Pang, K.J. Chon, O. Taratula, A multifunctional theranostic platform based on phthalocyanine-loaded dendrimer for image-guided drug delivery and photodynamic therapy, Mol. Pharm 10 (2013) 3946–3958, https://doi.org/10.1021/mp400397t.
[9] S.K. Marshall, P. Angsantikul, Z. Pang, N. Nasongkla, R.S.D. Hussen, S. D. Thamphiwatana, Biomimetic targeted theranostic nanoparticles for breast cancer treatment, Molecules (Basel, Switzerland) 27 (2022), https://doi.org/10.3390/MOLECULES27196473.
[10] P. Tagde, A. Najda, K. Nagpal, G.T. Kulkarni, M. Shah, O. Ullah, S. Balant, M. H. Rahman, Nanomedicine-Based Delivery Strategies for Breast Cancer Treatment and Management, *Int. J. Mol. Sci.* 23 (5) (2022), https://doi.org/10.3390/IJMS23052856.
[11] M.G. Archana, K.S. Anusree, B.S. Unnikrishnan, P.L. Reshma, H.P. Syama, J. Sreekutty, M.M. Joseph, T.T. Sreelekha, HER2 siRNA Facilitated gene silencing coupled with doxorubicin delivery: a dual responsive nanoplatform abrogates breast cancer, *ACS Appl. Mater. Interfaces* 16 (20) (2024) 25710–25726, https://doi.org/10.1021/ACSAMI.4C02532.
[12] M.M. Joseph, S.R. Aravind, S.K. George, R.K. Pillai, S. Mini, T.T. Sreelekha, Co-encapsulation of Doxorubicin with galactoxyloglucan nanoparticles for intracellular tumor-targeted delivery in murine ascites and solid tumors, *Transl. Oncol.* 7 (5) (2014) 525–536, https://doi.org/10.1016/J.TRANON.2014.07.003.
[13] M.M. Joseph, S.R. Aravind, S.K. George, K. Raveendran Pillai, S. Mini, T. T. Sreelekha, Anticancer activity of galactoxyloglucan polysaccharide-conjugated doxorubicin nanoparticles: Mechanistic insights and interactome analysis, European Journal of Pharmaceutics and Biopharmaceutics : Official Journal of Arbeitsgemeinschaft Fur Pharmazeutische Verfahrenstechnik e.V 93 (2015) 183–195, https://doi.org/10.1016/J.EJPB.2015.04.001.
[14] X. Ai, J. Mu, B. Xing, Recent Advances of Light-Mediated Theranostics, Theranostics 6 (2016) 2439–2457, https://doi.org/10.7150/thno.16088.
[15] A. Allegra, G. Penna, A. Alonci, V. Rizzo, S. Russo, C. Musolino, Nanoparticles in oncology: the new theragnostic molecules, Anticancer. Agents. Med. Chem 11 (2011) 669–686, https://doi.org/10.2174/187152011796817682.
[16] A. Demiral, S.İ. Goralı, H. Yılmaz, N. Verimli, M. Çulha, S.S. Erdem, Stimuli-responsive theranostic system: A promising approach for augmented multimodal imaging and efficient drug release, Eur. J. Pharm. Biopharm. 177 (2022) 9–23, https://doi.org/10.1016/j.ejpb.2022.05.021.
[17] A. Demiral, N. Verimli, S.İ. Goralı, H. Yılmaz, M. Çulha, S.S. Erdem, A Rational design of multi-functional nanoplatform: Fluorescent-based “off-on” theranostic gold nanoparticles modified with D-α-Tocopherol succinate, J. Photochem. Photobiol. B 222 (2021) 112261, https://doi.org/10.1016/j.jphotobiol.2021.112261.
[18] R. Di Corato, G. Béalle, J. Kolosnjaj-Tabi, A. Espinosa, O. Clément, A.K.A. Silva, C. Ménager, C. Wilhelm, Combining magnetic hyperthermia and photodynamic therapy for tumor ablation with photoresponsive magnetic liposomes, ACS. Nano 9 (2015) 2904–2916, https://doi.org/10.1021/nn506949t.
[19] Y. Hu, S. Mignani, J.-P. Majoral, M. Shen, X. Shi, Construction of iron oxide nanoparticle-based hybrid platforms for tumor imaging and therapy, Chem. Soc. Rev 47 (2018) 1874–1900, https://doi.org/10.1039/C7CS00657H.
[20] D. Liu, F. Yang, F. Xiong, N. Gu, The Smart Drug Delivery System and Its Clinical Potential, Theranostics 6 (2016) 1306–1323, https://doi.org/10.7150/thno.14858.
[21] Q. Zhang, W. Shan, C. Ai, Z. Chen, T. Zhou, X. Lv, X. Zhou, S. Ye, L. Ren, X. Wang, Construction of Multifunctional Fe(3)O(4)-MTX@HBc Nanoparticles for MR Imaging and Photothermal Therapy/Chemotherapy, Nanotheranostics 2 (2018) 87–95, https://doi.org/10.7150/ntno.21942.
[22] J. Mosayebi, M. Kiyasatfar, S. Laurent, Synthesis, Functionalization, and Design of Magnetic Nanoparticles for Theranostic Applications, Adv. Healthc. Mater 6 (2017), https://doi.org/10.1002/adhm.201700306.
[23] P. Agostinis, K. Berg, K.A. Cengel, T.H. Foster, A.W. Girotti, S.O. Gollnick, S. M. Hahn, M.R. Hamblin, A. Juzeniene, D. Kessel, M. Korbelik, J. Moan, P. Mroz, D. Nowis, J. Piette, B.C. Wilson, J. Golab, Photodynamic therapy of cancer: an update, CA Cancer J. Clin 61 (2011) 250–281, https://doi.org/10.3322/caac.20114.
[24] E. Ostańska, D. Aebisher, D. Bartusik-Aebisher, The potential of photodynamic therapy in current breast cancer treatment methodologies, Biomed. Pharmacother. 137 (2021) 111302, https://doi.org/10.1016/j.biopha.2021.111302.
[25] P. Majumdar, R. Nomula, J. Zhao, Activatable triplet photosensitizers: magic bullets for targeted photodynamic therapy, J. Mater. Chem. C 2 (2014) 5982–5997, https://doi.org/10.1039/C4TC00659C.
[26] G. Saranya, P. Anees, M.M. Joseph, K.K. Maiti, A. Ajayaghosh, A Ratiometric Near-Infrared Fluorogen for the Real Time Visualization of Intracellular Redox Status during Apoptosis, *Chemistry (weinheim an Der Bergstrasse, Germany)* 23 (30) (2017) 7191–7195, https://doi.org/10.1002/CHEM.201700839.
[27] S. Shamjith, M.M. Joseph, V.P. Murali, G.S. Remya, J.B. Nair, C.H. Suresh, K. K. Maiti, NADH-depletion triggered energy shutting with cyclometalated iridium (III) complex enabled bimodal Luminescence-SERS sensing and photodynamic therapy, *Biosens. Bioelectron.* 204 (2022), https://doi.org/10.1016/J.BIOS.2022.114087.
[28] N.W. Nompumelelo Simelane, C.A. Kruger, H. Abrahamse, Photodynamic diagnosis and photodynamic therapy of colorectal cancer in vitro and in vivo, RSC Adv. 10 (2020) 41560–41576, https://doi.org/10.1039/d0ra08617g.
[29] M.T. Olson, Q.P. Ly, A.M. Mohs, Fluorescence guidance in surgical oncology: challenges, opportunities, and translation, Mol. Imaging. Biol 21 (2019) 200–218, https://doi.org/10.1007/s11307-018-1239-2.
[30] M.A. Ahmadi, J.I. Lim, Pharmacotherapy of age-related macular degeneration, Expert. Opin. Pharmacother 9 (2008) 3045–3052, https://doi.org/10.1517/14656560802473480.
[31] B.W. Henderson, T.J. Dougherty, How does photodynamic therapy work? Photochem. Photobiol 55 (1992) 145–157, https://doi.org/10.1111/j.1751-1097.1992.tb04222.x.
[32] S. Michels, U. Schmidt-Erfurth, Photodynamic therapy with verteporfin: a new treatment in ophthalmology. Semin Ophthalmol 16:201-206, Semin. Ophthalmol 16 (2001) 201–206, https://doi.org/10.1076/soph.16.4.201.10298.
[33] N. Verimli, S.İ. Goralı, B. Abisoglu, C.L. Altan, B.O. Sucu, E. Karatas, A. Tulek, C. Bayraktaroglu, M.C. Beker, S.S. Erdem, Development of light and pH-dual responsive self-quenching theranostic SPION to make EGFR overexpressing micro tumors glow and destroy, J. Photochem. Photobiol. B 248 (2023) 112797, https://doi.org/10.1016/j.jphotobiol.2023.112797.
[34] C. Chen, Y.C. Cheng, C.H. Yu, S.W. Chan, M.K. Cheung, P.H.F. Yu, In vitro cytotoxicity, hemolysis assay, and biodegradation behavior of biodegradable poly (3-hydroxybutyrate)–poly(ethylene glycol)–poly(3-hydroxybutyrate) nanoparticles as potential drug carriers, *J. Biomed. Mater. Res. A* 87A (2) (2008) 290–298, https://doi.org/10.1002/JBM.A.31719.
[35] W. Chen, S. Park, C. Patel, Y. Bai, K. Henary, A. Raha, S. Mohammadi, L. You, F. Geng, The migration of metastatic breast cancer cells is regulated by matrix stiffness via YAP signalling, *Heliyon* 7 (2) (2021) e06252, https://doi.org/10.1016/j.heliyon.2021.e06252.
[36] MicroRNA expression profiles associated with the metastatic ability of MDA–MB–231 breast cancer cells. (n.d.). Retrieved December 31, 2024, from https://www.spandidos-publications.com/10.3892/ol.2023.13926.
[37] A. Parekh, D. Das, S. Das, S. Dhara, K. Biswas, M. Mandal, S. Das, Bioimpedimetric analysis in conjunction with growth dynamics to differentiate aggressiveness of cancer cells, Scientific Rep. 8 (1) (2018) 1–10, https://doi.org/10.1038/s41598-017-18965-9.
[38] A. Cahyadi, I. Ugrasena, M. Ratwita Andarsini, M. Larasati, A. Aryati, Relationship between Bax and Bcl-2 protein expression and outcome of induction phase chemotherapy in pediatric acute lymphoblastic leukemia, Asian. Pac. J. Cancer. Prev. 23 (2022) 1679–1685, https://doi.org/10.31557/APJCP.2022.23.5.1679.
[39] S. Karmakar, N.L. Banik, S.K. Ray, Curcumin suppressed anti-apoptotic signals and activated cysteine proteases for apoptosis in human malignant glioblastoma U87MG cells, *Neurochem. Res.* 32 (12) (2007) 2103–2113, https://doi.org/10.1007/S11064-007-9376-Z.
[40] L. Zhu, M.B. Han, Y. Gao, H. Wang, L. Dai, Y. Wen, L.X. Na, Curcumin triggers apoptosis via upregulation of Bax/Bcl-2 ratio and caspase activation in SW872 human adipocytes, *Mol. Med. Rep.* 12 (1) (2015) 1151–1156, https://doi.org/10.3892/MMR.2015.3450.
[41] B. Kulsoom, T.S. Shamsi, N.A. Afsar, Z. Memon, N. Ahmed, S.N. Hasnain, Bax, Bcl-2, and Bax/Bcl-2 as prognostic markers in acute myeloid leukemia: are we ready for Bcl-2-directed therapy? *Cancer. Manag. Res.* 10 (2018) 403–416, https://doi.org/10.2147/CMAR.S154608.